

Development of aerodynamic bearing support for application in air cycle machines

J. Šimek^{a,*}, P. Lindovský^b

^aTECHLAB Ltd., Sokolovská 207, 190 00 Praha, Czech Republic

^bPrvní brněnská strojírna V. Bíteš, a. s., Vlkovská 279, 595 12 Velká Bíteš, Czech Republic

Received 26 February 2014; received in revised form 6 June 2014

Abstract

Air cycle machines (ACM) are used in environmental control system of aircrafts to manage pressurization of the cabin. The aim of this work is to gain theoretical and experimental data enabling replacement of rolling bearings, which require lubrication and have limited operating speed, with aerodynamic bearing support. Aerodynamic bearings do not pollute process air and at the same time allow achieving higher operating speed, thus enabling to reduce machine mass and dimensions. A test stand enabling the verification of aerodynamic bearing support properties for prospective ACM was designed, manufactured and tested with operating speeds up to 65 000 rpm. Some interesting features of the test stand design and the test results are presented. A smaller test stand with operating speed up to 100 000 rpm is in design stage.

© 2014 University of West Bohemia. All rights reserved.

Keywords: air cycle machine, aerodynamic bearings, foil bearings, tilting pad journal bearings, elastically supported pads, spiral groove thrust bearings, rotor stability

1. Introduction

Former types of air cycle machines (ACM) had rotors supported in rolling bearings, which could not operate without lubrication. Traces of lubricant polluted the air, thus, endangering the crew and passengers. Moreover, working life of rolling bearings as well as their operating speed is limited, which prevents achieving higher speed and at the same time smaller ACM dimensions. In order to improve competitive advantages of machines produced by PBS V. Bíteš, a project of development ACM with aerodynamic bearings was started in 2012.

Most air cycle machines use foil bearings [1–3], which have some unique properties, namely possibility of adaptation to operating conditions and excellent dynamic properties due to additional damping caused by friction between the bearing and supporting foils (see Fig. 1) and between the supporting foil and the bearing casing. Both bearing and supporting foils are deformed by the generated aerodynamic pressure. As the bearing gap and at the same time bearing properties change with speed, it is relatively difficult to calculate bearing characteristics.

However, even better dynamic properties have tilting pad journal bearings with elastically supported pads (Fig. 2) described in detail in [4]. They combine excellent stability of tilting pad bearings, as a result of very small cross coupling stiffness terms, with positive properties of foil bearings, namely possibility to adapt itself to changed operating conditions and additional damping due to friction of elastic elements on bearing casing.

*Corresponding author. Tel.: +420 607 933 682, e-mail: j.simek@techlab.cz.

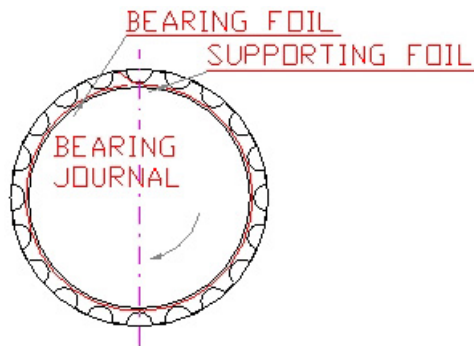


Fig. 1. Typical foil bearing

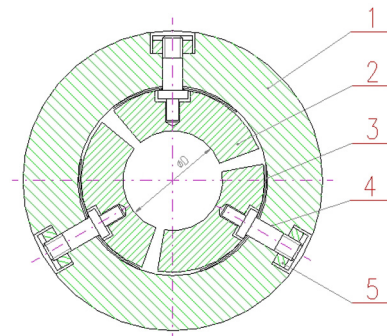


Fig. 2. Tilting pad bearing (ESTP)

As can be seen in the original design of ACM in Fig. 3, the rotor with the turbine (left) and blower (right) impeller was supported in two angular contact rolling bearings preloaded by the spring. Rolling bearings were replaced by aerodynamic journal bearings with elastically supported tilting pads (ESTP) and aerodynamic spiral groove thrust bearings.

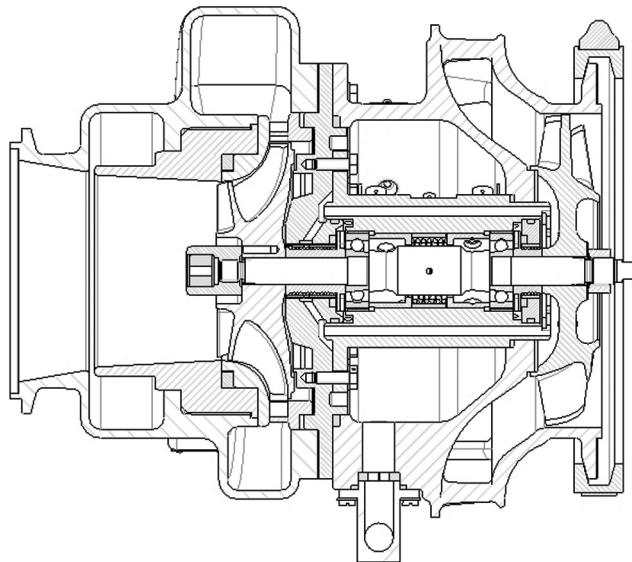


Fig. 3. Original ACM with rotor supported in rolling bearings

ACM designed as a test stand for verification of bearing properties [5] is presented in Fig. 4. The rotor is supported in two aerodynamic tilting pad bearings, and axial forces are taken up by double-sided aerodynamic spiral groove thrust bearing 4, 5. The bearing pads 3 are supported on the elastic elements 6, which are deformed to required shape by means of pins 7 and nuts 8. The difference between the inner radius of the bearing casing 2 and the outer radius of the pad enables the rolling of pads on elastic element inner surface, so that they can tilt in circumferential direction. The elastic elements are preloaded to such an extent that maximum pad load capacity exceeds the force necessary for elastic element deformation. In case that the bearing clearance is reduced to a dangerously low value, elastic elements make it possible to restore the bearing clearance back to its safe value. Friction between the elastic elements and bearing body contributes to the damping of a gas film, similarly as in the foil bearings. Moreover, the overall damping is further increased by the squeeze effect of gas pushed out of the gap between the elastic elements and the bearing body.

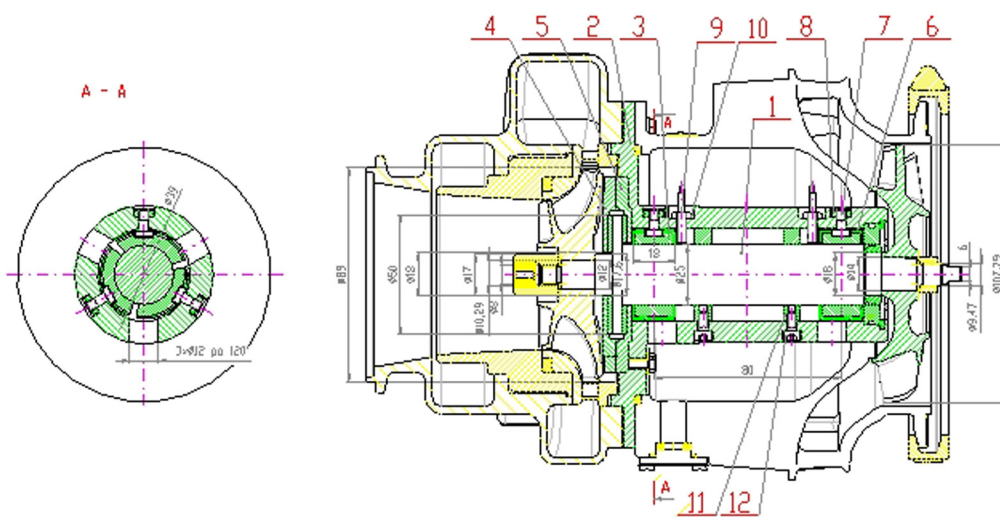


Fig. 4. Test stand with aerodynamic bearing support

The aerodynamic thrust bearings 4 a 5 substitute to some extent original labyrinth seal, because they prevent the air to flow from the turbine (left impeller) to the blower (right impeller) side. However, this was the cause of unexpected problems with the axial force magnitude. The maximum axial force directed to the turbine is higher than the axial load acting in the opposite direction and therefore, it is beneficial that the thrust bearing 4 could have bigger sliding surface (lower inner diameter) than the other one.

2. Calculation of bearing characteristics and rotor dynamics

The theoretical basis for the calculation of aerodynamic tilting pad bearing function properties is briefly described in [4]. Static and dynamic bearing characteristics are calculated with the computer programs “SATPJB” and “DATPJB”.

The journal bearings have the diameter of 25 mm and the width to diameter ratio of 0.72. Manufacturing clearance in the range 0.035 to 0.040 mm was selected due to relatively low speed. The Manufacturing clearance defined as $c_S = R_S - R_C$ is an important design parameter together with the bearing preload $\delta = 1 - c_L/c_S$, where $c_L = R_L - R_C$ (variable designation in Fig. 5).

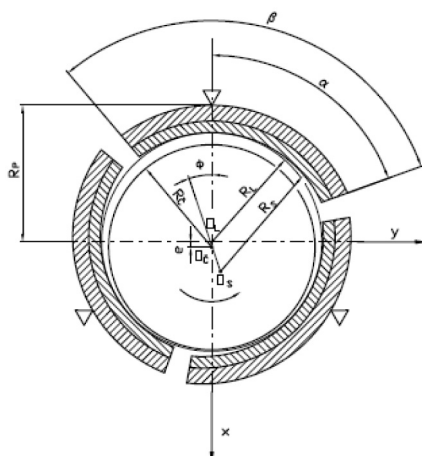


Fig. 5. TPJ bearing geometry

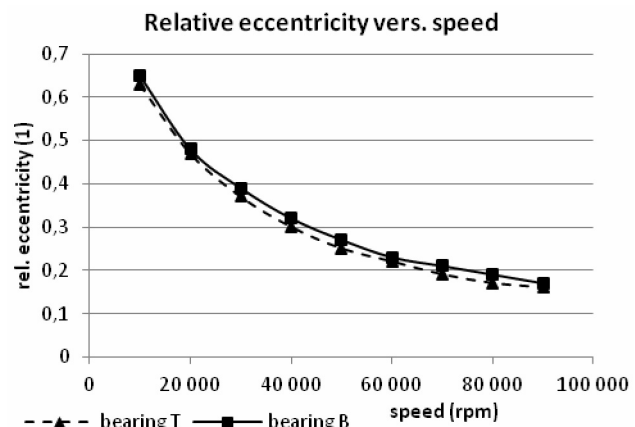


Fig. 6. Relative eccentricity in journal bearings

The diagram in Fig. 6 shows the relative eccentricity (eccentricity relative to the bearing clearance) of the journal in both bearings, which is almost the same because of not much differing load. It can be seen that with increasing speed, the relative eccentricity decreases to very small values — the journal centre is almost in the centre of the bearing.

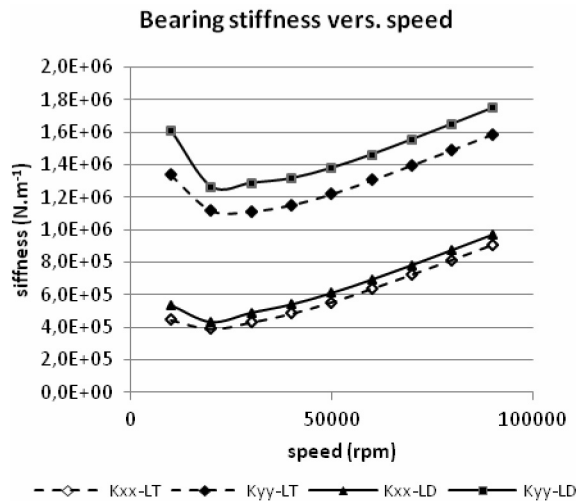


Fig. 7. Bearing stiffness coefficients

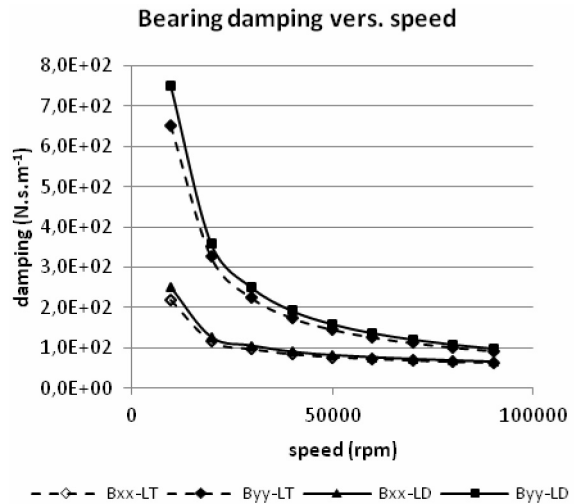


Fig. 8. Bearing damping coefficients

The bearing dynamic properties represented by the stiffness and damping coefficients calculated by the program “DATPJB” are shown in the diagrams in Figs. 7 and 8. Principal bearing stiffness and damping coefficients are shown in dependence on speed. It is evident that in contrast to the stiffness coefficients of hydrodynamic tilting pad bearings, aerodynamic bearings have the element K_{xx} lower than the K_{yy} one. It is due to the bearing geometry with only 3 pads, whereas the hydrodynamic bearings have 4 or 5 pads. With the exception of the lowest speeds, the bearing stiffness increases with increasing speed. The bearing damping is decreasing monotonously with increasing speed, which is standard for all sliding bearings. The calculated bearing stiffness and damping coefficients are used in the calculation of rotor dynamics.

Due to low damping, rotors in aerodynamic bearings cannot pass through the bending critical speed. Moreover, the 1st bending critical speed should be at least 60 % above the maximum operating speed; otherwise one could expect problems with excessive vibrations due to the start of rotor bending. This requirement and the achievement of rotor stability are, therefore, the two most important aspects of dynamic analysis [6]. The analysis showed four “bearing” critical speeds, i.e., critical speeds of rigid rotor on gas film, which are situated in the range from 6900 to 11900 rpm and are well damped. The rotor exhibits somewhat unorthodoxly positioned bending critical speeds, because apart from the 1st bending critical speed of counter-rotating precession at 113700 rpm, the next critical speed is counter-rotating precession with the 2nd bending mode at 197100 rpm. The 1st bending critical speed of co-rotating precession is at 261800 rpm, i.e., more than 400 % above the operating speed. According to the Campbell diagram in Fig. 9, the critical speeds of 113700 and 261800 rpm are two branches of one eigenvalue split by the gyroscopic moments. The vibration mode at 197100 rpm (not shown in the Campbell diagram) is the typical 2nd one (sine wave), while the vibration mode at 261800 rpm is typically the 1st one.

As is evident from Fig. 10, which shows the eigenvalue damping, real parts of the four lowest eigenvalues are negative, which means that the rotor operation is stable. The stability

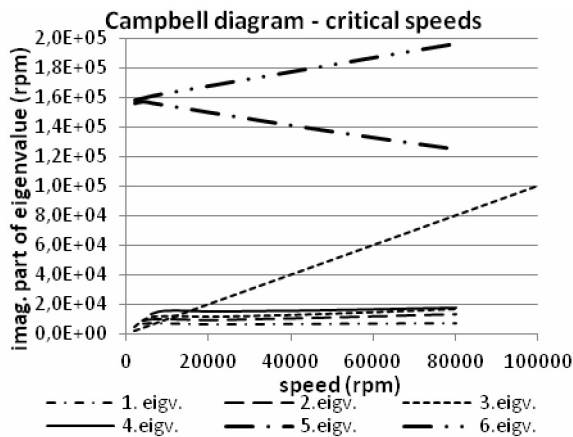


Fig. 9. Campbell diagram of critical speeds

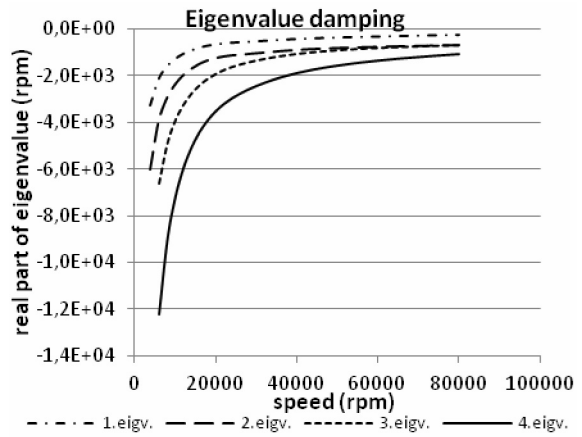


Fig. 10. Damping of critical speeds

reserve of the rotor is defined as

$$\chi = -2\text{Re}(\lambda)/\text{Im}(\lambda) \cdot 100 [\%],$$

where $\text{Re}(\lambda)$ and $\text{Im}(\lambda)$ are the real and imaginary parts of the eigenvalue, respectively.

At the speed of 60 000 rpm, the two lowest eigenvalues have the stability reserve of 10 % and 13.8 %, respectively, which should be quite sufficient for safe operation. The stability reserve of 10 % is generally considered to be safe for stable rotor operation. However, in some previous applications, rotors operated securely with stability reserve around 5 %. Rotor operability was also confirmed with a calculated response to unbalance. The residual unbalance for a rotor with the maximum operating speed of 60 000 rpm according to the class G2.5 of ISO 1940 standard is 0.38 g.mm. This unbalance was divided between the turbine and the blower impellers in ratio of their masses. The rotor response to static unbalance (unbalances in-phase) and dynamic unbalance (unbalances out-of-phase) in dependence on speed is shown in Figs. 11 and 12. It can be seen that up to 80 000 rpm, there is no resonance peak with the exception of the speed interval around 15 000 rpm with well damped critical speeds of rigid rotor on a gas film.

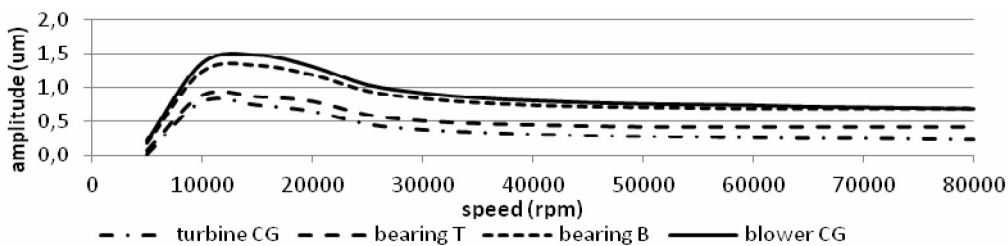


Fig. 11. Rotor response to static unbalance

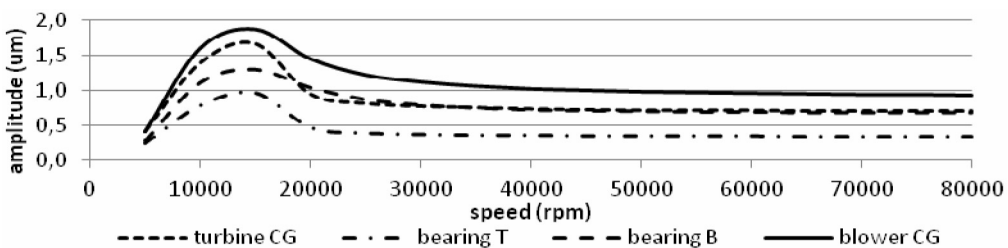


Fig. 12. Rotor response to dynamic unbalance

3. The 1st period of tests

As is evident from the cross section in Fig. 4, the test stand is equipped with relative sensors for the detection of rotor vibrations $\underline{9}$ located next to both journal bearings. There are two pairs of Micro-epsilon S04 sensors working on eddy current principle oriented 90° apart. This orientation enables to display the trajectory of rotor centre in the bearing. Because the rotor vibrations had very low level and the trajectories were distorted by disturbances, they were not evaluated. Beside radial vibrations of the rotor, excursions in axial direction were also followed by the eddy current sensor. Certain correlation between the axial shift and tilting of rotor axis can be observed [7]. Rotor run-up from about 9 000 to almost 17 000 rpm is shown in Fig. 13.

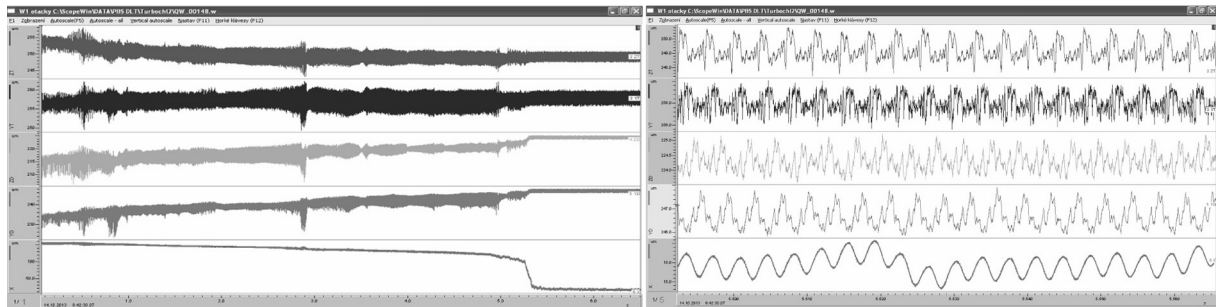


Fig. 13. Run-up of the rotor, generation of the full aerodynamic film at about 16 000 rpm

Top down in Fig. 13 and all following records of vibrations are signals:

- turbine bearing – horizontal direction,
- turbine bearing – vertical direction,
- blower bearing – horizontal direction,
- blower bearing – vertical direction,
- axial direction.

Expanded signals in the right diagram of Fig. 13 show a situation with a fully developed air film. Small disturbances can be seen in all vibration signals in the radial direction, which can be attributed to material properties changing around the shaft periphery. Fig. 14 presents rotor acceleration from 35 500 to 42 200 rpm. The change of axial force direction took place at about 39 000 rpm, which also brought about relatively great shift in the radial direction, such as the one in the bearing at the blower side. It shows that due to the pad elastic support with relatively low stiffness, the rotational axis can tilt so that thrust bearing and thrust runner sliding surfaces align to be parallel to each other.

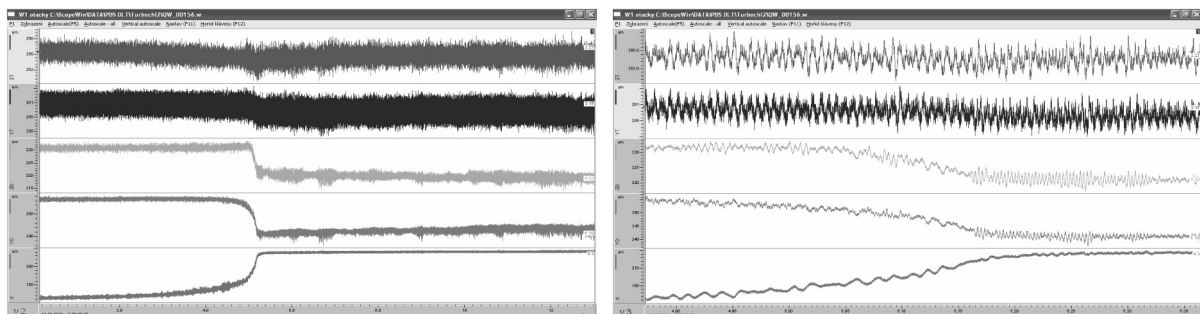


Fig. 14. Rotor acceleration from 35 500 to 42 200 rpm with change of axial force direction

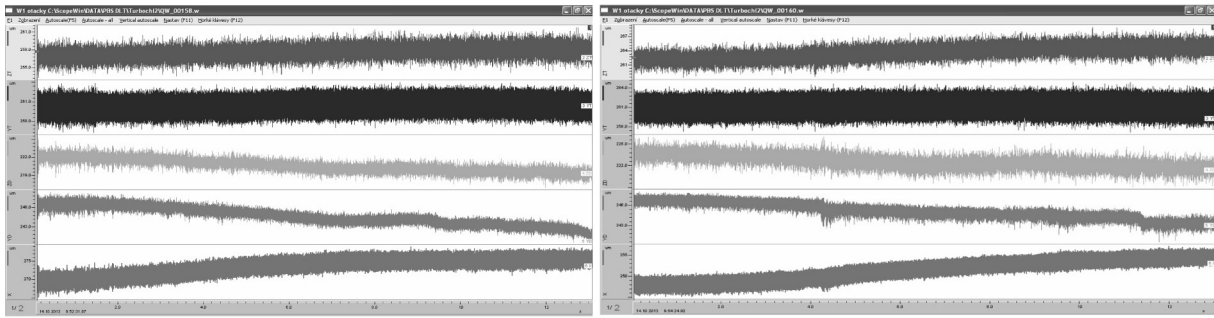


Fig. 15. Acceleration from 42 500 to 47 000 rpm and from 47 500 to 53 000 rpm

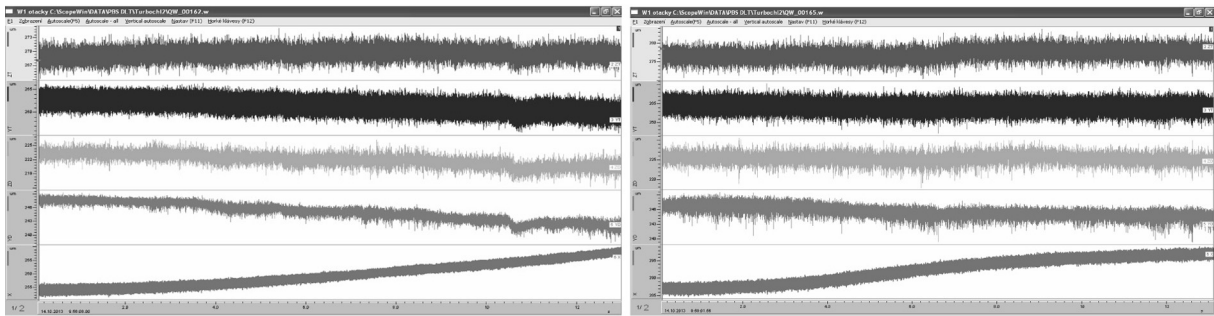


Fig. 16. Acceleration from 55 000 to 59 000 rpm and from 59 400 to 63 700 rpm

This is most important from the standpoint of thrust bearing load carrying capacity, which is very dependent on the parallelism of sliding surfaces. Tilting of rotational axis accompanying the change of axial force/axial shift can be also seen in Fig. 15 illustrating rotor acceleration from 42 500 to 47 000 rpm and from 47 500 to 53 000 rpm. The maximum radial shift occurs in horizontal direction. Similar rotor behaviour follows then the speed is increased from 55 000 to 59 000 rpm and from 59 400 to 63 700 rpm as shown in Fig. 16. Small increase in vibration amplitude can be seen in signals from the bearing on blower side, which could indicate that the thrust bearing load capacity is nearing its limit.

Although the operation speed was already achieved, it was decided to increase the speed once more. Results for acceleration from 62 800 to 66 600 rpm are shown in Fig. 17. Apart from further shift in the axial direction and a slight increase in vibration amplitude in blower bearing, there were no indications of potential problems. However, after a relatively short time, the vibration amplitude dramatically increased, as shown in the right part of Fig. 17. At this point, the machine was stopped and disassembled. Essential parts of the aerodynamic bearing support after failure are shown in Figs. 18 and 19.

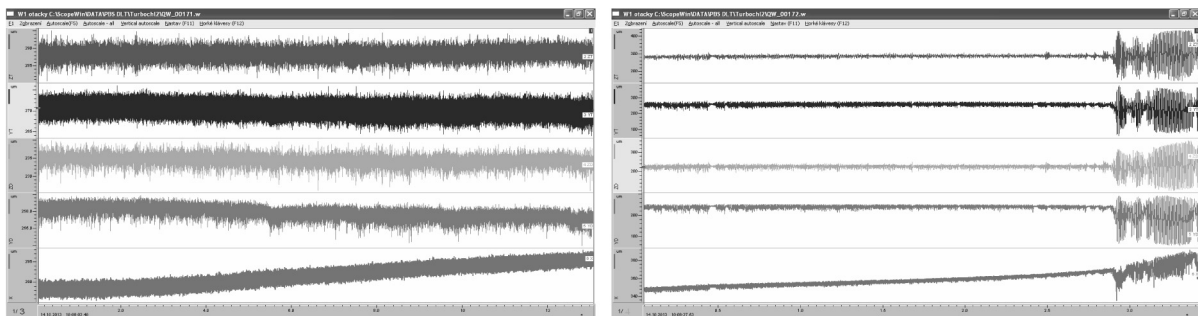


Fig. 17. Acceleration from 62 800 to 66 600 rpm; Beginning of failure at 65 000 rpm

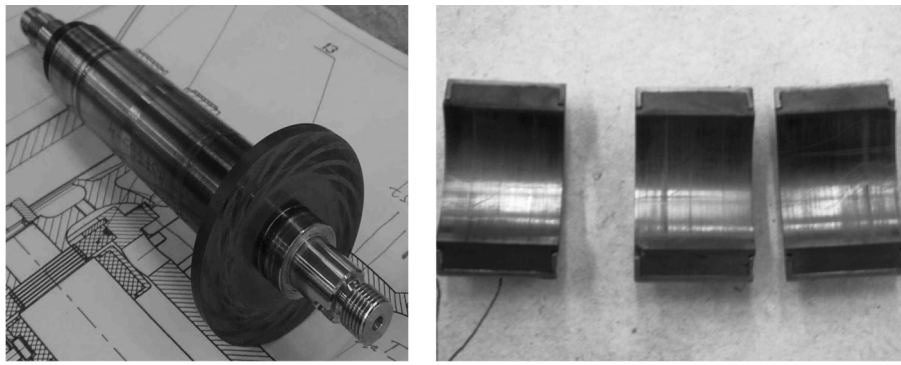


Fig. 18. Rotor with thrust disk and pads from journal bearing at blower side after failure

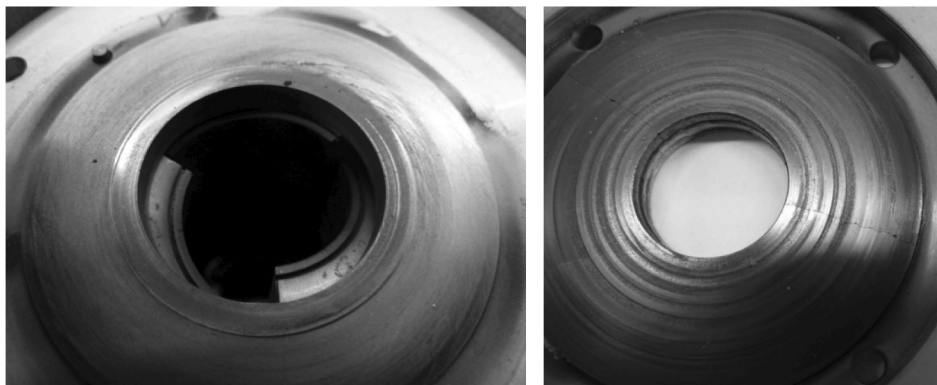


Fig. 19. Auxiliary (left) and main (right) thrust bearing after failure

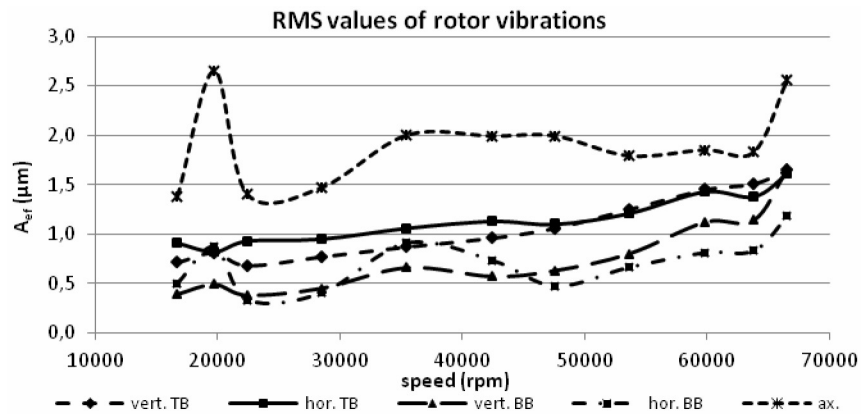


Fig. 20. RMS value of rotor vibration amplitude

It can be seen that the main thrust bearing with graphite lining as well as steel thrust disk on the rotor are heavily damaged by the mutual contact at sliding speed exceeding $170 \text{ m} \cdot \text{s}^{-1}$. On the other hand, the bearing pads and opposed sliding surfaces on the rotor were quite undamaged. The failure was apparently caused by the overloading of the main thrust bearing and the subsequent contact of sliding surfaces, which resulted in substantially increased vibrations in the journal bearings within the whole clearance (including clearance of elastically supported pads in bearing casing).

As is evident from diagram in Fig. 20, the rotor vibrations up to 67 000 rpm were quite low. Curves in Fig. 20 represent the RMS values of relative vibrations in horizontal, vertical and axial directions in bearings on blower (BB) and turbine (TB) side. No RMS value of rotor

vibration amplitude in radial direction exceeded $2\ \mu\text{m}$. Vibrations in axial direction were lower than $3\ \mu\text{m}$ in the whole speed range. These data reflect the very good level of rotor balancing as well as the proper function of both the journal and thrust bearings. The only indication of thrust bearing overloading was the very slight vibration increase in the journal bearing at blower side.

According to calculation, the main thrust bearing was operating with gas film thickness lower than $3\ \mu\text{m}$, which is an extremely low value for a bearing 50 mm in diameter. The axial force acting on the thrust bearing is a resultant of pressures acting on the impellers and the unloaded part of the thrust disk. Change of axial force direction at about 40 000 rpm was caused by pressure increase at the turbine side, which was then amplified by the pressure acting on the other (now unloaded) side of the thrust disk. The development of axial force with speed is shown in diagram in Fig. 21. As can be seen from the diagram, at the speed of 65 000 rpm axial force exceeded value of 150 N, scheduled for bearing design, almost three times. The change of axial force direction around 40 000 rpm was confirmed by the measured data.

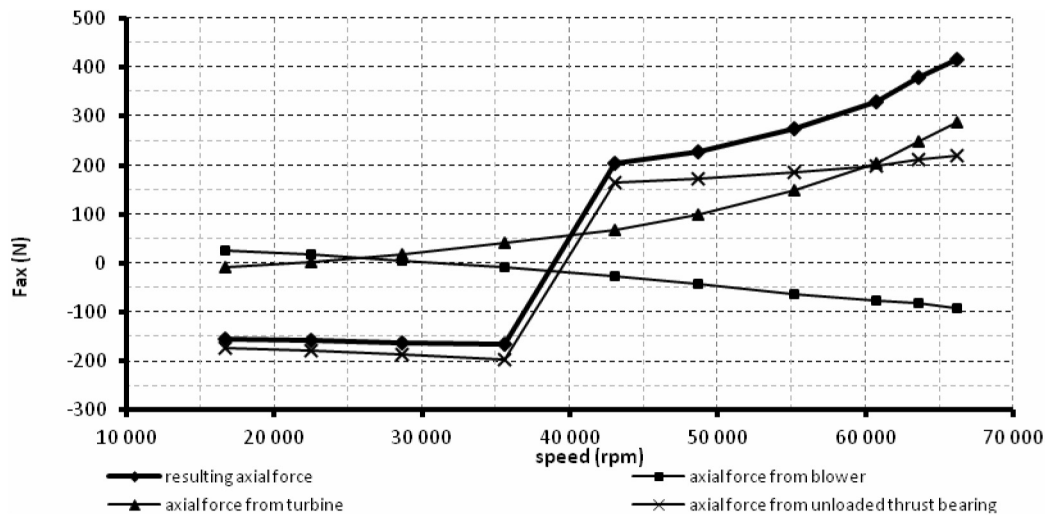


Fig. 21. Calculated axial force

4. Test stand modifications and new series of tests

An axial force analysis showed that it is necessary to reduce the thrust bearing load [8]. Labyrinth seal was, therefore, installed behind the turbine impeller (see Fig. 22). The tests continued by sequentially increasing the speed with similar rotor vibrations as in the previous tests. Sam-

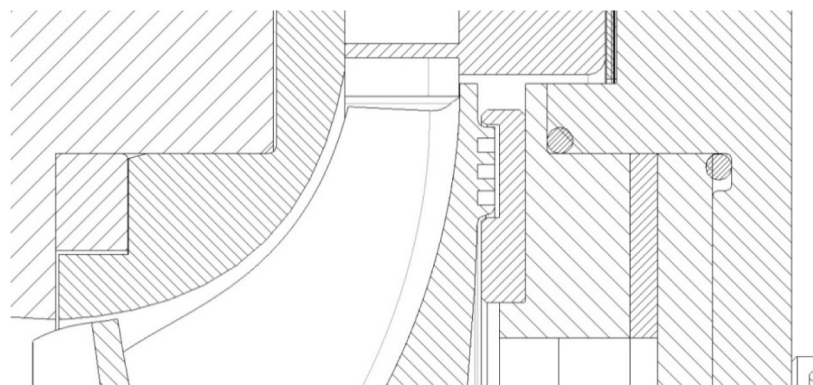


Fig. 22. Labyrinth seal behind the turbine impeller

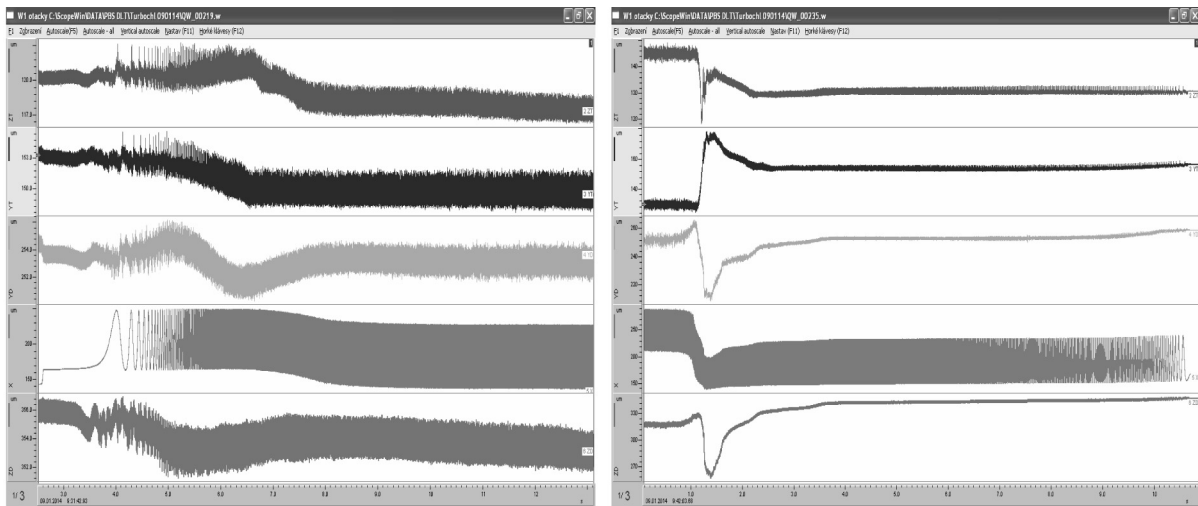


Fig. 23. Run up to 23 000 rpm and run-down from 65 000 rpm

ples of vibration signals are presented in Fig. 23. The sequence of vibration signals is the same as in the previous tests, with the exception of axial direction, which is now the 2nd one from below. The axial signal is distorted by the damage of measured surface during disassembly. There is an eccentric hole, which “provides” virtual axial vibration with amplitude of about 70 μm . It is practically impossible to assess real amplitude of axial vibrations, but axial shifts of the rotor can be still observed. Fig. 23 shows rotor run-up from stand-still to about 23 000 rpm with axial shift around 40 μm and relatively big shifts in all radial directions. The right part of Fig. 23 presents rotor run-down from maximum speed to practical stand-still. It can be seen that the change of axial force direction takes place between 59 000 rpm and 48 000 rpm. However, no change of axial force direction was encountered with increasing speed.

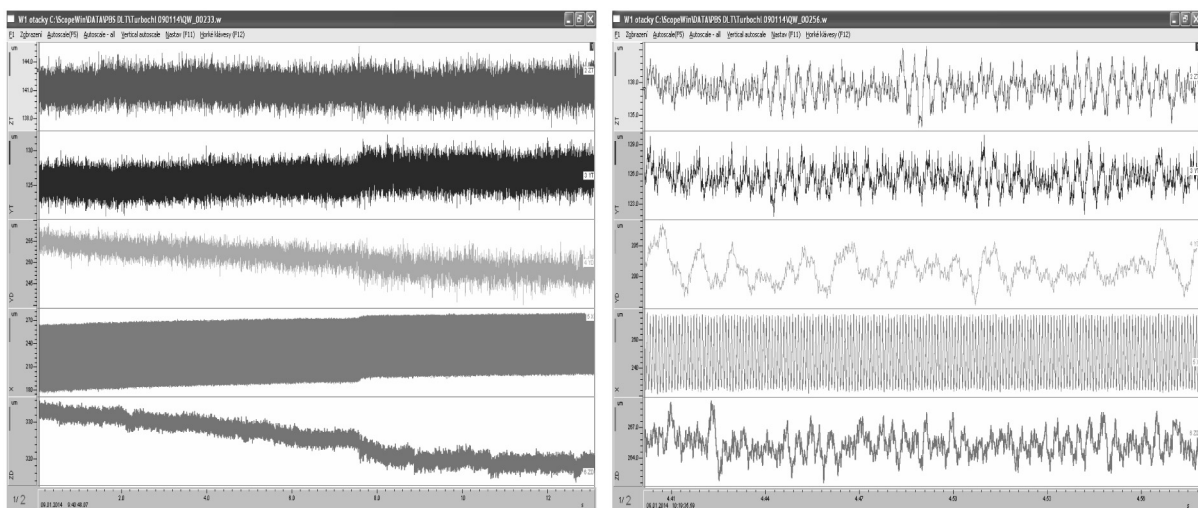


Fig. 24. Increasing speed from 57 500 to 60 200 rpm; Stable maximum speed of 65 000 rpm

Due to labyrinth seal, the axial force was significantly reduced; it still increases with increasing speed, as evident from the left part of Fig. 24 (the right part of axial force signal is higher than the left one – the rotor shifted to the blower side). However, the maximum calculated value of axial load was about 235 N; with this load value, the main thrust bearing works with a film thickness of 5 μm . The right part of Fig. 24 shows vibration signals at the stable

maximum speed of about 65 000 rpm. The peak to peak vibration amplitudes of all signals in radial direction did not exceed 5 μm . The RMS values of vibration amplitudes in radial direction in dependence on speed are presented in Fig. 25. Sensor at the blower side in horizontal direction (dotted line in Fig. 25) was damaged during the rotor failure in the 1st test and its characteristics cannot be considered as quite correct. The other 3 sensors show RMS values of vibration amplitude lower than 1.5 μm in the whole speed range, i.e., extremely small values for such a high speed.

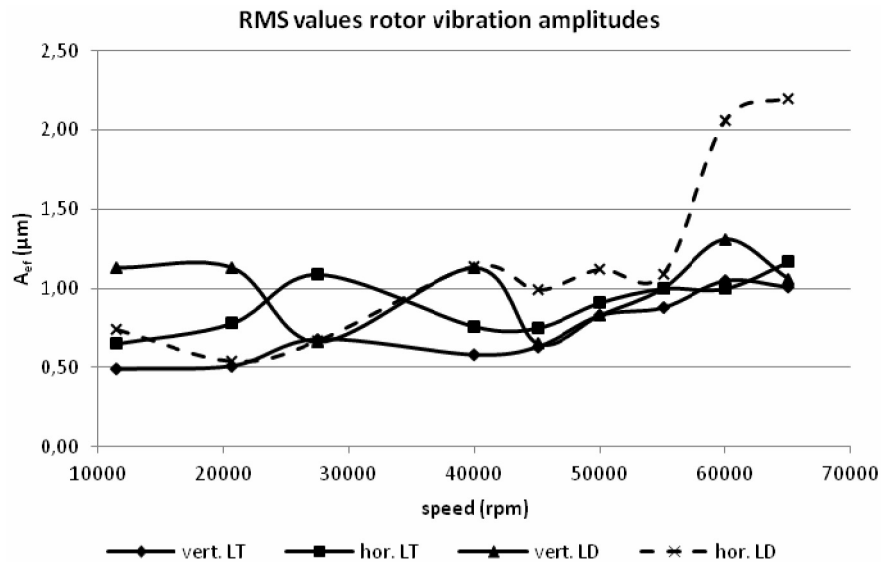


Fig. 25. RMS values of rotor vibration amplitude in radial direction vs. speed

5. Final tests and machine disassembly

Final tests consisted of run-up and run-down cycles and of cycling from minimum speed to maximum speed. In the 1st part of the test, the machine completed 1 000 cycles from standstill to the maximum speed of 60 000 rpm with a 1 minute-long run followed by a run-down to stand still. The 2nd part of the test consisted of 500 cycles of 5 minute run at 30 000 rpm, increasing speed to 60 000 rpm, 5 minute run at this speed, and again decreasing speed to 30 000 rpm etc. After finishing the 2nd test, the machine was disassembled. Two important facts were found out when examining the bearing parts:

1. A small amount of oil from the system of pressurized air driving the machine penetrated into main thrust bearing, as documented in Fig. 26. The oil mixed with the graphite particles loosened from the bearing lining significantly increased the starting torque during the rotor run-up. The presence of oil at the graphite lining is by no means desirable and does not reduce the wear of sliding surfaces during the run-up and run-down; it has rather the opposite effect.
2. Some of the nuts securing the pad position and by that also basic bearing clearance were completely or partly loosened. Pertinent pads were then pressed by their elastic supports to the shaft so that the bearing support lost its biggest advantage in comparison with the foil bearings, in the form of a low starting torque. On the other hand, it showed that the tilting pad bearings with elastically supported pads can operate in the same way as the foil bearing, i.e., without basic bearing clearance. Similarly as in the foil bearings, the pads are separated from the shaft surface and a full gas film is generated when the rotor achieves certain speed.



Fig. 26. Main thrust bearing and thrust disk polluted by the mixture of oil and graphite particles

It is quite natural that during the start up with traces of oil in the thrust bearing gap, the rotor exhibited high level of vibration before a full air film was established. It is documented in the left part of Fig. 27, showing the run-up from standstill to about 20 000 rpm. The vibration amplitudes around $200\ \mu\text{m}$ p-p in radial direction (practically in the range of the whole bearing clearance including the clearance of pads in bearing casing) are apparently caused by the contact of sliding surfaces in the auxiliary thrust bearing, which is preloaded by the main thrust bearing operating in the “hydrodynamic” regime (i.e., with oil as a process medium). As soon as the oil is thrown out of the thrust disk and a complete gas film is established in the auxiliary thrust bearing, the vibration level drops to the usual level of around $4\ \mu\text{m}$ p-p. With a further speed increase, there is no increase in vibration level, only shifts in the radial direction as the rotor aligned with the main thrust bearing sliding surface. Almost steady shift in the axial direction to the turbine impeller (last but one signal) indicates growing axial force with increasing speed.

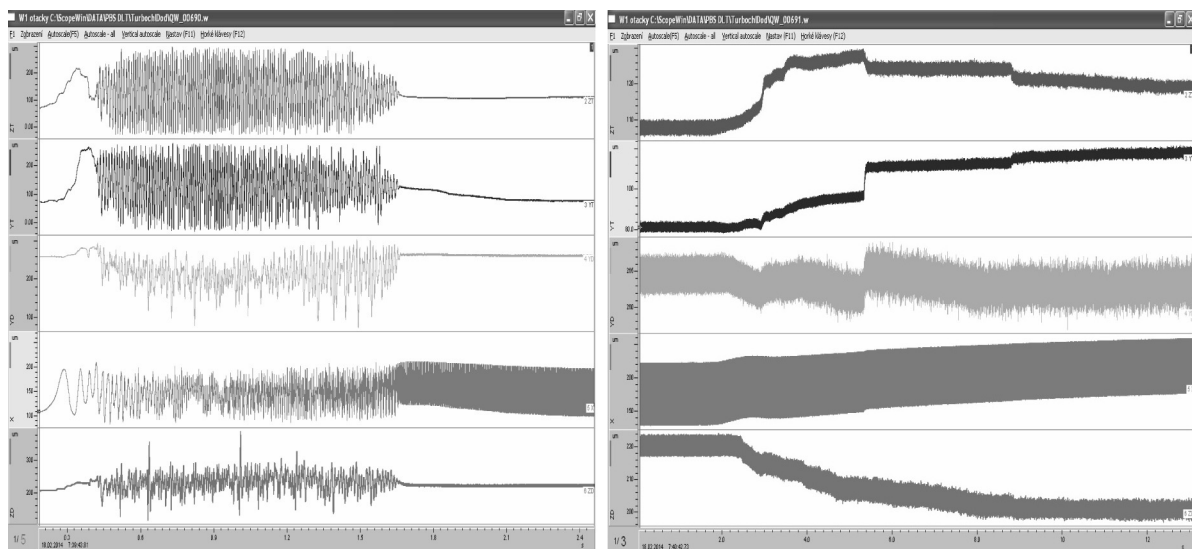


Fig. 27. Run-up from standstill to about 20 000 rpm (left); Speed increase from about 20 000 to 50 300 rpm (right)

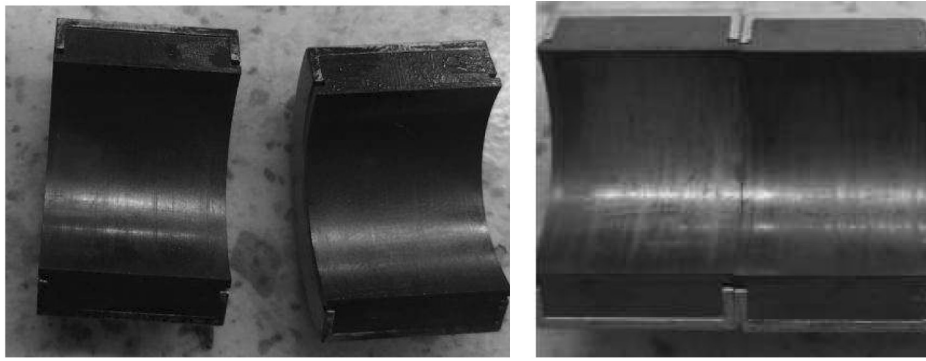


Fig. 28. Bearing pads at the turbine side (left) and blower side (right) after disassembly



Fig. 29. Cleaned rotor

As can be seen from Fig. 28, the bearing pads at the turbine side (next to the thrust bearing) were also somewhat polluted by oil in contrast to the pads from the bearing at the blower side, which stayed quite clean. After shaft cleaning, it is evident that the sliding surfaces are not damaged and neither on the thrust disk and neither on the shaft at the journal bearing locations (see Fig. 29). Traces at the outer diameter of the thrust disk indicate that there was a slight and very short contact of sliding surfaces, but the damage is very small and the rotor and bearings are able to operate further quite satisfactorily.

6. Conclusions

An air cycle machine (ACM) with rolling bearing rotor support was reconstructed and used as a test stand for the verification of air bearing properties. The 1st part of the test proved operability of the air bearing support, consisting of elastically supported tilting pad journal bearings and spiral groove thrust bearings, up to maximum speed of 65 000 rpm. The failure occurred due to excessive axial force, which exceeded the nominal value for thrust bearing design almost three times.

Installation of a labyrinth seal behind the turbine impeller proved effective in reducing the axial load to its maximum value about 235 N, with which main thrust bearing works with film thickness about 5 μm . Up to the maximum speed of 65 000 rpm, the rotor runs with RMS values of vibration amplitudes up to 1.5 μm , which corresponds to peak-to-peak values lower than 4.5 μm . Such a small values of rotor vibration confirm correct function of bearing support and a very good level of rotor balancing.

The aerodynamic bearing support operability and reliability was further confirmed by a series of 1 000 starts and stops and 500 cycles of acceleration from 30 000 rpm to 60 000 rpm and back to 30 000 rpm.

A smaller ACM with maximum operating speed of 95 000 rpm was designed and is prepared for manufacture (Fig. 30), as machine dimensions and weight are the most important parameters for flight applications.

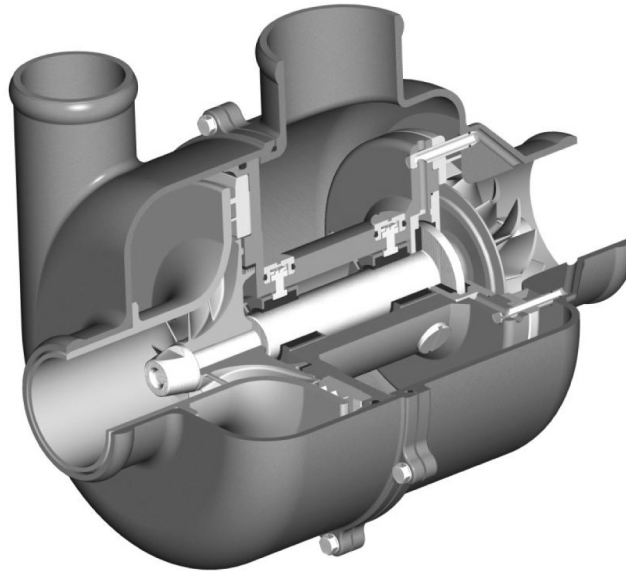


Fig. 30. Design of a smaller ACM variant

Acknowledgements

This work was supported by the Technology Agency of the Czech Republic under project PID TA02011295 “Verification of air bearing technology”.

References

- [1] Agrawal, L., Foil air/gas bearing technology — an overview, ASME publication 97-GT-347.
- [2] Howard, S. A., Bruckner, R. J., DellaCorte, CH., Radil, K. C., Gas foil bearing technology advancement for Brayton cycle turbines, NASA/TM-2007-214470.
- [3] Howard, S. A., Bruckner, R. J., Radil, K. C., Advancement towards oil-free rotorcraft propulsion, NASA/TM-2010-216094.
- [4] Šimek, J., Application of a new type of aerodynamic bearing in power gyroscope, *Engineering Mechanics* 19 (5) (2012) 359–368.
- [5] Šimek, J., Design of aerodynamic bearing support of the test stand, Technical report TECHLAB No. 12–417, 2012. (in Czech)
- [6] Šimek, J., Design of the test stand for verification of air bearing technology, Technical report TECHLAB No. 12–420, 2012. (in Czech)
- [7] Šimek, J., Experimental verification of air bearing properties, Technical report TECHLAB No. 13–413, 2013. (in Czech)
- [8] Šimek, J., Experimental verification of air bearing properties. Phase 2 — after reduction of axial force, Technical report TECHLAB No. 14–401, 2014. (in Czech)